Nuclear Medicine and Biology 124-125 (2023) 108383

Contents lists available at ScienceDirect

Nuclear Medicine and Biology

journal homepage: www.elsevier.com/locate/nucmedbio

Comparison of three ^{18}F-labeled 2-nitroimidazoles for imaging hypoxia in breast cancer xenografts: [^{18}F]FBNA, [^{18}F]FAZA and [^{18}F]FMISO

Sofia Nascimento dos Santos [a,1], Melinda Wuest [b,1], Hans-Sonke Jans [b], Jenilee Woodfield [b], Arian Pérez Nario [a], Daniel Krys [b], Jennifer Dufour [b], Darryl Glubrecht [b], Cody Bergman [b], Emerson Soares Bernardes [a,2], Frank Wuest [b,*,2]

[a] Radiopharmacy Center, Nuclear and Energy Research Institute (IPEN / CNEN - SP), CEP 05508-000 São Paulo, SP, Brazil
[b] Department of Oncology, University of Alberta, Cross Cancer Institute, Edmonton T6G 2R7, Alberta, Canada

ARTICLE INFO

Keywords:
Positron emission tomography
Hypoxia
[18F]FBNA
[18F]FAZA
[18F]FMISO

ABSTRACT

Background: Tumour hypoxia is associated with increased metastasis, invasion, poor therapy response and prognosis. Most PET radiotracers developed and used for clinical hypoxia imaging belong to the 2-nitroimidazole family. Recently we have developed novel 2-nitroimidazole-derived PET radiotracer [^{18}F]FBNA (*N*-(4-[^{18}F]fluoro-benzyl)-2-(2-nitro-1*H*-imidazol-1-yl)-acet-amide), an ^{18}F-labeled analogue of antiparasitic drug benznidazole. The present study aimed to analyze its radio-pharmacological properties and systematically compare its PET imaging profiles with [^{18}F]FMISO and [^{18}F]FAZA in preclinical triple-negative (MDA-MB231) and estrogen receptor-positive (MCF-7) breast cancer models.

Methods: In vitro cellular uptake experiments were carried out in MDA-MB321 and MCF-7 cells under normoxic and hypoxic conditions. Metabolic stability *in vivo* was determined in BALB/c mice using radio-TLC analysis. Dynamic PET experiments over 3 h post-injection were performed in MDA-MB231 and MCF-7 tumour-bearing mice. Those PET data were used for kinetic modelling analysis utilizing the reversible two-tissue-compartment model. Autoradiography was carried out in tumour tissue slices and compared to HIF-1α immunohistochemistry. Detailed *ex vivo* biodistribution was accomplished in BALB/c mice, and this biodistribution data were used for dosimetry calculation.

Results: Under hypoxic conditions *in vitro* cellular uptake was elevated in both cell lines, MCF-7 and MDA-MB231, for all three radiotracers. After intravenous injection, [^{18}F]FBNA formed two radiometabolites, resulting in a final fraction of 65 ± 9 % intact [^{18}F]FBNA after 60 min p.i. After 3 h p.i., [^{18}F]FBNA tumour uptake reached SUV values of 0.78 ± 0.01 in MCF-7 and 0.61 ± 0.04 in MDA-MB231 tumours (both $n = 3$), representing tumour-to-muscle ratios of 2.19 ± 0.04 and 1.98 ± 0.15, respectively. [^{18}F]FMISO resulted in higher tumour uptakes (SUV 1.36 ± 0.04 in MCF-7 and 1.23 ± 0.08 in MDA-MB231 (both $n = 4$; $p < 0.05$) than [^{18}F]FAZA (0.66 ± 0.11 in MCF-7 and 0.63 ± 0.14 in MDA-MB231 (both n = 4; n.s.)), representing tumour-to-muscle ratios of 3.24 ± 0.30 and 3.32 ± 0.50 for [^{18}F]FMISO, and 2.92 ± 0.74 and 3.00 ± 0.42 for [^{18}F]FAZA, respectively. While the fraction per time of radiotracer entering the second compartment (k3) was similar within uncertainties for all three radiotracers in MDA-MB231 tumours, it was different in MCF-7 tumours. The ratios k3/(k3 + k2) and K1*k3/(k3 + k2) in MCF-7 tumours were also significantly different, indicating dissimilar fractions of radiotracer bound and trapped intracellularly: K1*k3/(k2 + k3) [^{18}F]FMISO (0.0088 ± 0.001)/min, $n = 4$; $p < 0.001$) > [^{18}F]FAZA (0.0052 ± 0.002)/min, n = 4; $p < 0.01$) > [^{18}F]FBNA (0.003 ± 0.001)/min, $n = 3$). In contrast, in MDA-MB231 tumours, only K1 was significantly elevated for [^{18}F]FMISO. However, this did not result in significant differences for K1*k3/(k2 + k3) for all three 2-nitroimidazoles in MDA-MB231 tumours.

Conclusion: Novel 2-nitroimidazole PET radiotracer [^{18}F]FBNA showed uptake into hypoxic breast cancer cells and tumour tissue presumably associated with elevated HIF1-α expression. Systematic comparison of PET imaging performance with [^{18}F]FMISO and [^{18}F]FAZA in different types of preclinical breast cancer models

* Corresponding author.
E-mail address: wuest@ualberta.ca (F. Wuest).
[1] Equally contributed to this work.
[2] Shared last authorship.

https://doi.org/10.1016/j.nucmedbio.2023.108383
Received 27 March 2023; Received in revised form 24 August 2023; Accepted 25 August 2023
Available online 26 August 2023

revealed a similar tumour uptake profile for [^{18}F]FBNA with [^{18}F]FAZA and, despite its higher lipophilicity, still a slightly higher muscle tissue clearance compared to [^{18}F]FMISO.

1. Introduction

Hypoxia represents a general pathological condition characterized by a reduced oxygen supply to a particular tissue or organ [1]. Up to 60 % of solid tumours display hypoxic and/or anoxic areas resulting from the imbalance between oxygen supply and oxygen consumption [2]. Hypoxia in solid tumours results from abnormal and chaotic vascularization in tumour tissue, limiting the increased oxygen demand of a growing tumour mass [3]. Oxygen deprivation drives tumours to develop adaptive responses to low-oxygen conditions, resulting in altered gene expression and overall cell metabolism changes that contribute to their survival in an unfavourable environment [4]. Most downstream gene expression changes and cellular adaptation mechanisms induced by hypoxic conditions are mediated by the transcription factor HIF-1α [5]. More than 1500 HIF target genes have been identified, causing malignant reprogramming, leading to metabolic adaptation, invasion, metastasis, and angiogenesis [6]. Therefore, tumour hypoxia is linked to increased metastasis and invasion, poor response to radiotherapy and chemotherapy, and poor prognosis [1].

Several non-invasive molecular imaging techniques have evolved over the past three decades to assess and visualize tumour hypoxia in preclinical and clinical studies. Prominent examples include positron emission tomography (PET), single photon emission computed tomography (SPECT), magnetic resonance imaging (MRI), and optical imaging. [7,8]. Functional imaging with PET is a valuable tool to analyze and quantify tissue hypoxia *in vivo* in preclinical and clinical settings [9,10].

Most radiotracers for PET imaging of hypoxia belong to the 2-nitroimidazole compound family since the original introduction of [^{18}F]fluoromisonidazole ([^{18}F]FMISO) in 1986, one of the most widely used radiotracers for hypoxia imaging [9,11–13].

As a 2-nitroimidazole, [^{18}F]FMISO passively diffuses across the cell membrane and is reduced by nitroreductase enzymes in the cytoplasm. This process is reversible when cells are well-oxygenated. However, under hypoxic conditions, [^{18}F]FMISO is reduced stepwise, leading to the progressive production of R-NHOH compounds that bind covalently to intracellular proteins causing metabolic trapping of the radiotracer [14]. The time for passive diffusion, intracellular reduction and trapping is crucial for good image contrast.

[^{18}F]FMISO readily crosses cell membranes, but it also displays a slow clearance from normal tissue, which results in longer times ($\geq$ 3 h) to achieve acceptable tumour/background ratios, which are typically in the range of 1.2–1.4 [15,16].

Therefore, a next-generation of 2-nitroimidazoles was developed, as exemplified with [^{18}F]fluoroazomycin arabinoside ([^{18}F]FAZA) [17]. The lower lipophilicity of [^{18}F]FAZA provided higher image contrast due to a faster clearance from non-target tissues compared to [^{18}F]FMISO [18,19]. However, questions about the reproducibility and variability of the [^{18}F]FAZA-PET data, especially in clinical settings, remain open [20].

Besides [^{18}F]FMISO and [^{18}F]FAZA, other radiofluorinated nitroimidazole-based radiotracers have been developed, including [^{18}F]fluoroerythronitroimidazole ([^{18}F]FETNIM) [21], [^{18}F]fluoroetanidazole ([^{18}F]FETA) [22], and several more lipophilic fluoroalkyl acetamide derivatives such as 2-(2-nitroimidazol-1-yl)-*N*-3-[^{18}F]fluoropropyl acetamide [^{18}F]EF1, 2-(2-nitroimidazol-1-yl)-*N*-(3,3,3-[^{18}F]trifluoro-propyl)acetamide [^{18}F]EF3 and 2-(2-nitro-1Himidazol-1-yl)-*N*-(2,2,3,3,3-[^{18}F]pentafluoropropyl)-acet-amide ([^{18}F]EF5) [16]. The higher lipophilicity of fluoroalkyl acetamides [^{18}F]EF1, [^{18}F]EF3, and [^{18}F]EF5 enable fast cell membrane penetration resulting in the rapid uptake of the radiotracers in most tissues and organs, including the central nervous system [11,23].

Discussions concerning the feasibility of ^{18}F-labeled 2-nitroimidazoles for imaging glioblastomas tend to favour the use of [^{18}F]EF5 for its ability to readily cross the blood-brain barrier, whereas [^{18}F]FAZA is only suitable in cases where the integrity of the blood-brain barrier is disrupted [11]. However, despite all the potential benefits of the different ^{18}F-labeled 2-nitroimidazoles developed, to date, there are no significant advantages over [^{18}F]FMISO [24].

Recently, we have developed *N*-(4-[^{18}F]fluorobenzyl)-2-(2-nitro-1*H*-imidazol-1-yl)-acetamide ([^{18}F]FBNA), an ^{18}F-labeled analogue of antiparasitic drug benznidazole, as a novel 2-nitroimidazole derivative for hypoxia PET imaging (Fig. 1) [25].

Benznidazole is currently used to treat *Chagas* disease caused by the parasitic protozoan *Trypanosoma cruzi*. As a 2-nitroimidazole compound, benznidazole becomes an active cytotoxic agent upon biological reduction mediated by nitro-reductases, demonstrating promising cell-killing capacity in hypoxic tumour cells [26].

The goal of the present study was to *A)* analyze the radiopharmacology of 2-nitro-imidazole [^{18}F]FBNA and *B)* systematically compare the PET imaging profiles of [^{18}F]FBNA, [^{18}F]FMISO and [^{18}F]FAZA (Fig. 1) in triple-negative breast cancer (MDA-MB231) lacking estrogen receptor (ER), progesterone receptor (PR) and human epidermal growth factor receptor 2 (HER2) as well as estrogen receptor-positive breast cancer (MCF-7). The intention was to examine if the three hypoxia radiotracers would result in potential differences between each other and between the two different breast cancer models.

2. Materials and methods

2.1. Chemicals and radiosynthesis

Radiosynthesis of [^{18}F]fluoroazomycin arabinoside ([^{18}F]FAZA), [^{18}F]fluoromiso-nidazole ([^{18}F]FMISO), and 4-[^{18}F]fluorobenzylamine ([^{18}F]FBAmine) were performed on a GE TRACERlab™ FX (General Electric Company, Fairfield, CT, U.S.A.), fully automated synthesis unit (ASU). For [^{18}F]FAZA, 1-(2,3-diacetyl-5-tosyl-(α-D-arabinofuranosyl)-2-nitroimidazole, and for [^{18}F]FMISO, 1*H*-imidazole-1-propanol, 2-nitro-β-[(tetrahydro-2*H*-pyran-2-yl)oxy]-, 4-methyl benzenesulfonate (ester) (NITTP), were used as labeling precursors (both purchased from ABX Advanced Biochemical Compounds, Radeberg, Germany). The radiosynthesis of [^{18}F]FAZA and [^{18}F]FMISO was accomplished according to published procedures [27,28]. Synthesis of *N*-(4-[^{18}F]fluorobenzyl)-2-(2-nitro-1*H*-imidazol-1-yl)-acetamide ([^{18}F]FBNA) was performed manually starting from [^{18}F]FBAmine as per our recently published procedure [25]. All radiotracers were obtained in high radiochemical purity >99 %. The determined molar activities were 300 GBq/μmol for [^{18}F]FAZA, 34 GBq/μmol for [^{18}F]FMISO, and 7 GBq/μmol for [^{18}F]FBNA. The automated synthesis unit (ASU) was installed in a Comecer hot cell (Rolling Meadows, IL, USA). High-performance liquid chromatography (HPLC) analysis and purification of the radiolabeled products were performed using a Phenomenex LUNA® C18(2) column (100 Å, 250 × 10 mm, 10 μm) using gradient elution specific to the given

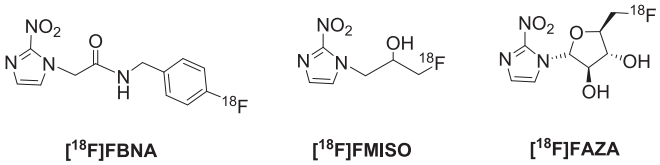

[^{18}F]FBNA [^{18}F]FMISO [^{18}F]FAZA

Fig. 1. Structures of ^{18}F-labeled 2-nitroimidazoles [^{18}F]FBNA, [^{18}F]FMISO and [^{18}F]FAZA.

compound (Gilson 321 pump, 171 diode array detector, Berthold Technologies Herm LC). Radio-TLC was performed using EMD. Merck F254 silica gel 60 aluminum-backed thin-layer chromatography (TLC) plates (Bioscan AR-2000). Water was obtained from a Barnstead Nanopure water filtration system (Barnstead Diamond Nanopure pack organic free RO/DIS).

Kryptofix 4,7,13,16,21,24-Hexaoxa-1,10-diazabicyclo[8.8.8]-hexacosane ($K_{2.2.2.}$) was purchased from T.C.I. America (Portland, OR, USA).

Unless otherwise stated and used as received from the supplier, the chemicals not stated above were obtained from Sigma-Aldrich® or Millipore Sigma (Oakville, ON, Canada).

2.2. In vitro cell uptake experiments

Human MCF-7 (ATCC HBT-22) and MDA-MB231 (ATCC HTB-26) breast cancer cells were grown in DMEM/F-12 (Thermo Fisher Scientific) with 10 % fetal bovine serum (Thermo Fisher Scientific) and 1 % penicillin/ streptomycin (10,000 U/mL).

For experiments, cells were seeded in 12-well plates in their medium and grown for 24 h. For experiments under hypoxic conditions, the medium was preconditioned for 3–4 h in a special hypoxia chamber at 1 % O_2 and 5 % CO_2 at 37 °C as described previously [29] and used to exchange the growth medium for the cells under hypoxia and compared with cells under normoxic conditions. Before the cell uptake experiments, the medium was removed 1 h before the experiment, and cells were washed two times with PBS and incubated in Krebs-Ringer buffer (120 mM NaCl, 4 mM KCl, 1.2 mM KH_2PO_4, 2.5 mM $MgSO_4$, 25 mM $NaHCO_3$, 70 mM $CaCl_2$, pH 7.4) for 1 h at 37 °C. Next, 300 μL Krebs-Ringer solution with 0.1–0.5 MBq of either ^{18}F-labeled 2-nitroimidazole was added to each well. Plates were incubated at 37 °C for specific time points (60, 120 and 180 min). Radiotracer uptake was stopped with 1 mL ice-cold PBS, and cells were washed two times with PBS and lysed in 0.4 mL lysis buffer (50 mM Tris, 150 mM NaCl, 0.1 % SDS, 0.5 % sodium deoxycholate, 0.5 % Triton X-100).

Radioactivity in cell lysates was measured as counts per minute using a Wizard 2 automatic γ-counter (PerkinElmer, Waltham, MA, USA). Data were normalized to 100 % control uptake under normoxic conditions and determined from 2 to 3 experiments in triplicates (3 wells per timepoint and experiment).

2.3. In vivo metabolic stability

The radiotracer solution containing 20 to 25 MBq [^{18}F]FBNA, [^{18}F]FMISO, or [^{18}F]FAZA in 8–10 % EtOH/saline was injected intravenously into female BALB/c mice under isoflurane anesthesia. Blood samples from the tail vein (20–40 μL) were collected at 5, 15, 30, 45 and 60 min post-injection.

Blood cells were separated by centrifugation (Mini Hettich centrifuge, Germany; 5 min, 13,000 RPM) followed by plasma protein precipitation using methanol (two parts per one part plasma) and a second centrifugation step (5 min, 13,000 RPM). Radioactivity in blood cell and plasma protein fractions and the supernatant was analyzed using a WIZARD2 Automatic gamma counter (PerkinElmer; Waltham, MA, USA) and calculated as % of total radioactivity in all three fractions. Supernantant was further analyzed by radio thin-layer chromatography (radio-TLC). Radio-TLC was used to analyze the radiometabolic profile as it allows for 100 % recovery especially when used for small radiolabeled molecules such as 2-nitroimidazole. Radio-TLCs were developed in 1:1 EtOAc/ethanol for [^{18}F]FBNA, [^{18}F]FMISO, or [^{18}F]FAZA resulting in R_f values of 0.6–0.7 and analyzed using a BAS-5000 reader.

2.4. Dynamic PET imaging

All animal experiments were carried out following the Canadian Council on Animal Care (CCAC) guidelines and approved by the local animal care committee of the Cross Cancer Institute. Human MCF-7 cells (5×10^6 cells in 100 μL PBS/Matrigel 50:50) or MDA-MB231 cells (5×10^6 cells in 100 μL PBS) were injected subcutaneously into the left shoulder of 8–10-week-old female NIH-III nude mice (20–22 g, Charles River, Saint-Constant, QC, Canada). MCF-7-bearing mice also received a subcutaneously implanted 0.72 mg/pellet containing estrogen in a 60-day release preparation (Innovative Research of America, Sarasota, FL, USA) into the upper right flank. Tumours were grown for 3 to 4 weeks, reaching 300–500 mm^3 sizes. General anesthesia of tumour-bearing mice was induced with inhalation of isoflurane in 40 % oxygen/60 % nitrogen (gas flow = 1 mL min − 1), and the mice were placed fixed in a prone position.

The body temperature was kept constant at 37 °C for the entire experiment. The mice in a prone position were placed in the center of the field-of-view (FOW) of an Inveon® PET/CT scanner (Siemens Preclinical Solutions, Knoxville, TN, USA). A transmission scan for attenuation correction was not acquired. The mice were injected with 5–7 MBq of either [^{18}F]FBNA, [^{18}F]FMISO or [^{18}F]FAZA in 100–200 μL of saline (0.9 %) containing 8 to 10 % ethanol through a tail vein catheter. Data acquisition was performed over 180 min in a 3D list mode. The dynamic list mode data were sorted into sinograms with 65-time frames (10×2, 8×5, 6×10, 6×20, 8×60, 10×120, 5×300, and 12×600 s). The frames were reconstructed using maximum *a posteriori* (MAP) as reconstruction mode. The pixel size was $0.085 \times 0.085 \times 0.121$ mm^3 ($256 \times 256 \times 63$), and the resolution at the axial center of the field of view was about 1.8 mm [30]. No correction for partial volume effects was applied. The image files were processed using the ROVER v 2.0.51 software (A.B.X. GmbH, Radeberg, Germany). Masks defining 3D regions of interest (ROI) were set, and the ROIs were defined as a threshold of 50 % SUV_{max} within an ellipsoid mask around the tumour on an image representing the average of the last 40 min of the acquisition (*i.e.* excluding the tracer uptake phase).

Mean standardized uptake values [SUV]mean = (activity/ mL tissue)/(injected activity/body weight), mL/g, were calculated for each ROI. All semi-quantified PET data are presented as means ± SD. Time-activity curves (TACs) were constructed using Graph-Pad Prism 5.0 (GraphPad Software).

2.5. Radiotracer kinetic analysis

Tracer kinetic analysis was performed using dynamically acquired PET imaging data with an established reversible two-tissue compartment model as described previously in the literature for [^{18}F]FAZA [31,48,49]. A volume of interest (VOI) was defined for the tumour using the Rover software (A.B.X. GmbH, Dresden, Germany) by applying a 50 % threshold as described above.

Image-derived input functions were obtained from regions around the heart, defined by the injected blood bolus visible in the first few time frames of the dynamic acquisitions, using a threshold of 50 % of SUV_{max} in that region. Four kinetic parameters (K1, k2, k3, k4) and the fractional blood volume (fbv), which account for the non-zero vascular space within the tumour ROI, describe the model. The analysis was carried out by fitting the measured tumour time-activity curves (TACs) with a two-exponential model of the general form:

$$TAC_{tumor} = (1 - fbv)\cdot(A_1 exp(-\alpha_1 t) + A_2 exp(-\alpha_2 t)) \otimes TAC_{blood} + fbv\cdot TAC_{blood} \quad (1)$$

where $\otimes$ denotes convolution and fbv, A_1, α_1, A_2, α_2 are fit parameters, the latter four representing the amplitude and time dependence of the exponentials [31]. The fit of Eq. (1) to the experimentally acquired tumour TACs was implemented in Matlab (The Mathworks, Inc., v. R2014b), utilizing a Nelder-Mead simplex direct search. The fit was governed by minimizing the sum over all time points of square differences between the measured values and the model prediction.

Metabolism during the measurement time plays a minor role for [^{18}F]MISO and [^{18}F]FAZA but needs to be accounted for in the case of

[^{18}F]FBNA.

Here, a metabolite analysis yielded the percentage of the intact tracer as a function of time (see Fig. 3). This data was extrapolated to time zero and parameterized by a biexponential fit. Lastly, this fitted curve was used to scale the image-derived input functions at each time point accordingly before performing the kinetic analysis.

2.6. Biodistribution of [^{18}F]FBNA

After intravenous injection of 1.5–4.5 MBq of [^{18}F]FBNA in saline with 10 % ethanol (100 to 150 μL) into the tail vein of isoflurane-anesthetized BALB/c mice, animals were allowed to regain consciousness until sacrifice.

While under isoflurane anesthesia, animals were euthanized at 5, 30 and 60 min, 3 h and 6 h post-injection and rapidly dissected. Organs of interest, including blood, heart, lung, liver, kidneys, spleen, stomach, duodenum, small intestine, upper and lower large intestine, pancreas, right femur, muscle, ovaries, brain, fat, thymus, uterus and urinary bladder were collected and weighed. Radioactivity in all tissues was measured in a WIZARD γ-counter (Wallac 1480 Wizard-3, Perkin-Elmer, Waltham, MA, USA) and results were analyzed as the percentage of injected dose per gram of tissue (%ID/g).

2.7. Radiation dosimetry analysis for [^{18}F]FBNA

Radiation dosimetry analysis for the determination of the normal organ-absorbed doses and the effective dose was performed using OLINDA/EXM software (version 1.1, Vanderbilt University, Nashville, TN, USA). Scaling of the animal-obtained values to human values was carried out by weighing the organ uptake with the relative organ mass in the animal and human:

$$\left(\frac{\%ID}{organ}\right)_{human} = \left(\frac{\%ID}{organ}\right)_{rat} \cdot \left[\left(\frac{m_{organ}}{m_{body}}\right)_{humam} \Big/ \left(\frac{m_{organ}}{m_{body}}\right)_{rat}\right] \quad (2)$$

In practice, concentrations $\left(\frac{\%ID}{organ}\right)_{rat} / (m_{organ})_{rat} \equiv \left(\frac{\%ID}{m_{organ}}\right)_{rat}$ are determined experimentally.

This also accounts for organs that cannot be excised in their entirety, such as muscle, blood and bone. Eq. 2 then becomes

$$\left(\frac{\%ID}{m_{organ}}\right)_{human} = \left(\frac{\%ID}{m_{organ}}\right)_{rat} \cdot \frac{(m_{body})_{rat}}{(m_{body})_{human}} \quad (3)$$

The values for $(\%ID/m_{organ})_{human}$ are obtained by first averaging the values $(\%ID/m_{organ})_{rat} \cdot (m_{body})_{rat}$ for the three individual animals sacrificed at each time point and then dividing by the adult human's weight of 73.7 kg [32,33].

To obtain the cumulated activity in each organ, these curves were multiplied by the human organ mass, using the values implemented in the OLINDA/EXM code [32], and integrated: for the first 6 h numerically by evaluating the area under the measured curve and beyond 6 h by fitting a mono-exponential function to the last four data points of each curve and integrating it from 6 h to infinity.

Not in all cases did the organs for which cumulated activity was determined through the biodistribution (see above) correspond to the source organs as defined in OLINDA/EXM. The following assumptions were made to derive the cumulated activity for the OLINDA-defined source organs: (i) It was assumed that all activity detected in the stomach, intestines and urinary bladder originated from their contents. (ii) Since exact quantities of the small amounts of bone and muscle activity contained in the remainder of the body were unknown, they were not subtracted from the whole body activity. (iii) The activity of the heart's content was determined from the blood concentration (decays/mL) and multiplied by the internal volume of the heart (510 mL, ICRP89). (iv) It was assumed that activity is uniformly distributed to cortical and trabecular bone and red marrow. The number of decays in each is assigned according to their weight ratio, based on the weight of the human skeleton of 10.45 kg (ICRP89), the ratio of cortical to the trabecular bone of 4/1 and the fact that red marrow constitutes 4 % of the total body mass [33,34]. The values determined for cumulated activity in each source organ were then used as input for the OLINDA/EXM code.

2.8. Autoradiography and immunohistochemistry

For autoradiography, MCF-7 or MDA-MB231 tumour-bearing NIH-III mice were injected with 20–25 MBq of either [^{18}F]FBNA, [^{18}F]FMISO or [^{18}F]FAZA in 8–10 % EtOH/saline into the tail vein again. After 2 h post-injection, mice were euthanized, and tumour tissue was harvested. Tumour tissue was embedded into Tissue-Tek embedding medium for frozen tissue specimens to ensure the optimal cutting temperature (OCT) and frozen in liquid nitrogen. Cryoslices of 40 μm were cut using a Leica CM1850 cryostat (Leica Microsystems Inc. Concorde, Ontario, Canada). Slices were placed into a BAS Cassette (2325, Fujifilm) and exposed to a phosphor imaging plate (BAS-MS 2025, Fujifilm) for ~60 min at room temperature and analyzed using a Typhoon 9400 Variable Mode Imager from molecular dynamics (GE Amersham Pharmacia Biotech, Amersham, UK).

Immunohistochemistry for the detection of HIF-1α, tumour slices were carried out on the cryo slices immediately adjacent to those used for autoradiography. Upon thawing, tissue sections were fixed with formalin for 30 min. The fixed sections were blocked overnight at 4 °C using 0.12 mg/mL unconjugated goat anti-mouse Fab fragments (115-003-007, Jackson Immunoresearch, West Grove, PA, USA) in 0.5 % fish skin gelatin (G7765, Sigma-Aldrich), pH 7.4, supplemented with 0.1 % Triton X-100.

The sections were rinsed three times with Tris-buffered saline (TBS; 200 mM Tris and 1500 mM NaCl according to Sigma-Aldrich) having 0.5 % Tween 200 (TBST) for 5 min each and then incubated with the rabbit polyclonal anti-HIF1α IgG (1:50, NB100449; Novus Biologicals, Oakville, ON, Canada) overnight at 4 °C in a humidity chamber. The samples were then treated with 3 % H_2O_2 in deionized water for 15 min, proceeded by three 10 min washes using TBST.

2.9. Statistical analysis

All data are expressed as means ± SD from n experiments. Graphs were constructed using Graph-Pad Prism 5.0 (GraphPad Software). Were applicable, statistical differences were tested using paired and unpaired Student's *t*-test and were considered significant at $p < 0.05$.

3. Results

Fig. 1 shows the molecular structure of the three ^{18}F-labeled 2-nitroimidazoles used in the present study: *N*-(4-[^{18}F]fluorobenzyl)-2-(2-nitro-1*H*-imidazol-1-yl)-acetamide ([^{18}F]FBNA), [^{18}F]fluoromisonidazole ([^{18}F]FMISO) and [^{18}F]fluoroazomycin arabinoside ([^{18}F]FAZA). Radiosynthesis of [^{18}F]FBNA was accomplished manually, as recently published by our group [26]. The synthesis of [^{18}F]FMISO and [^{18}F]FAZA have been adopted to automated radiosynthesis procedures (see Methods section).

3.1. In vitro cell uptake experiments in breast cancer cell lines

Cell uptake of 2-nitroimidazoles [^{18}F]FBNA, [^{18}F]FMISO, and [^{18}F]FAZA were carried out in the human estrogen receptor-positive MCF-7 cells as well as in the human triple-negative MDA-MB231 cells under normoxic and hypoxic (1 % O_2) conditions. Fig. 2 summarizes these results.

Under normoxic conditions, all three radiotracers showed uptake levels between ~1.5 to 4.5 % radioactivity/mg protein at 180 min independent of the cell line as they only enter the cells by passive

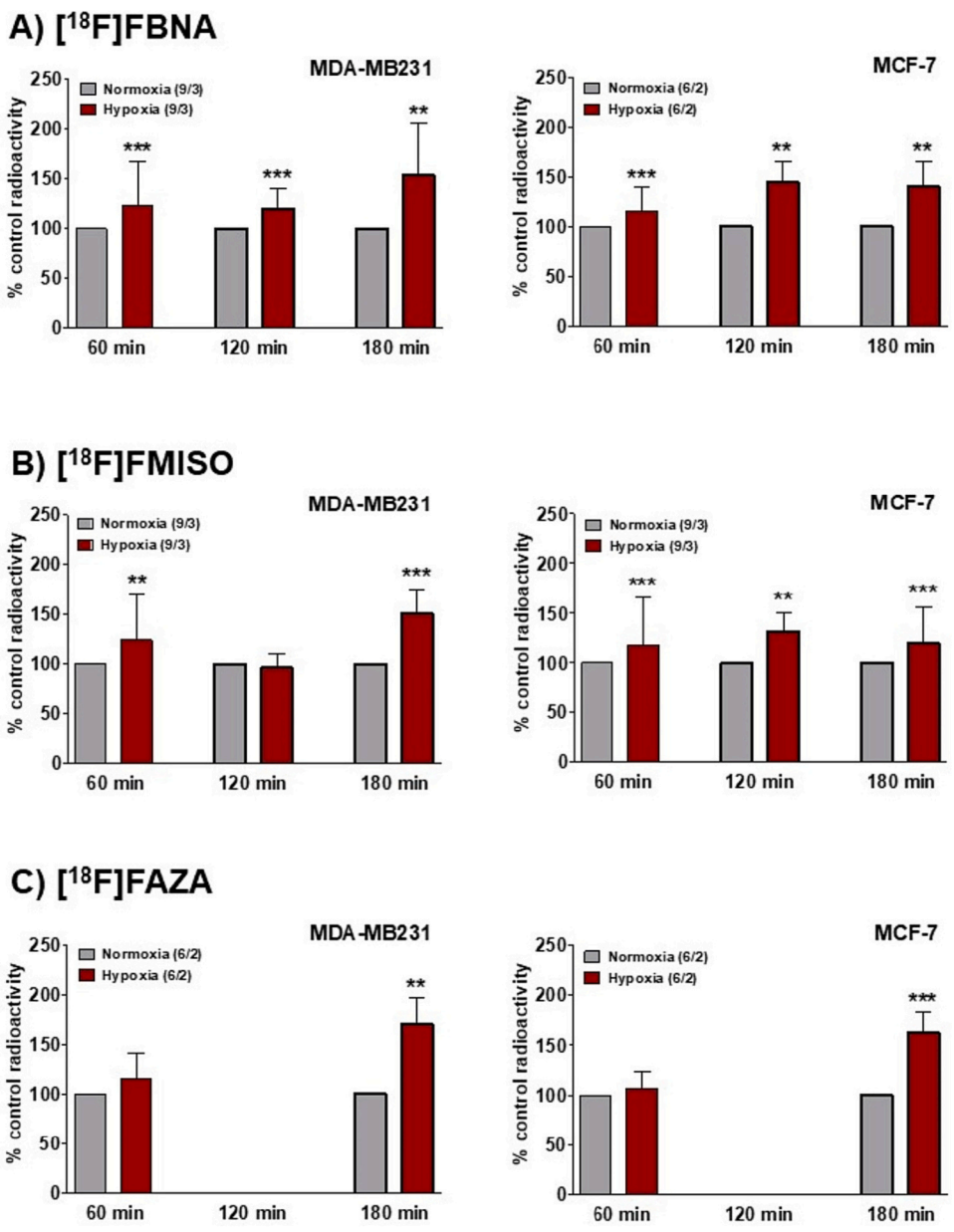

Fig. 2. *In vitro* radiotracer cell uptake of A) [^{18}F]FBNA, B) [^{18}F]FMISO and C) [^{18}F]FAZA into breast cancer cells MCF7 and MDA-MB231. Analysis of the effects of hypoxia (1 % O_2) in Comparison with uptake under normal control conditions. *In vitro* cell uptake was determined at 60, 120 and 180 min incubation time points. Data are shown as means ± SD from 2 to 3 different experiments; all experiments were performed in triplicate (6–9 data points from 2 to 3 experiments). * $p < 0.05$; ** $p < 0.01$; *** $p < 0.001$.

diffusion. Under hypoxic conditions, all three 2-nitroimidazoles showed a significant increase in uptake into MCF-7 cells, especially after 180 min (3 h) incubation time: [^{18}F]FBNA from 2.87 ± 0.28 to 3.98 ± 0.31 % radioactivity/mg protein (+40 %; $n = 6/2$ (6 wells from 2 experiments); $p < 0.01$); [^{18}F]FMISO from 1.26 ± 0.22 to 1.39 ± 0.18 % radioactivity/mg protein (+20 %; $n = 9/3$; $p < 0.05$) and [^{18}F]FAZA from 4.80 ± 0.44 to 7.66 ± 0.48 % radioactivity/mg protein (+62 %; n = 9/3; $p < 0.001$), respectively.

A similar pattern was observed in MDA-MB231 cells: [^{18}F]FBNA from 5.03 ± 0.71 to 8.41 ± 1.31 % radioactivity/mg protein (+54 %; n = 9/3; p < 0.05); [^{18}F]FMISO from 3.02 ± 0.81 to 4.74 ± 1.34 % radioactivity/mg protein (+51 %; n = 9/3; p < 0.05) and [^{18}F]FAZA from 4.96 ± 0.54 to 7.56 ± 1.24 % radioactivity/mg protein (+70 %; n = 9/3; p < 0.01). The *in vitro* cell uptake data showed that hypoxic conditions increase cell uptake of all three 2-nitroimidazoles, confirming that they function as hypoxia radiotracers.

3.2. *In vivo stability*

Blood compartment distribution and *in vivo* metabolic stability of [^{18}F]FBNA was analyzed in blood samples from BALB/c mice and compared to those from [^{18}F]FMISO and [^{18}F]FAZA (Fig. 3).

[^{18}F]FBNA is detected more in blood cells (~60 %) *versus* plasma (~35–40 %), not changing much over the time course of the experiment, while [^{18}F]FAZA is found at similar levels in blood cells and plasma (~50 % each).

Analysis of [^{18}F]FMISO revealed slightly more variable results between 5, 15, 30 and 60 min post injection). Overall, after 60 min post-injection, the plasma protein-bound fraction (precipitated from the supernatant after the 1st centrifugation step) was 7.9 ± 1.6 % ($n = 3$) for [^{18}F]FBNA after plasma protein precipitation, which was similar to [^{18}F]FMISO (8 %, $n = 1$) but higher than [^{18}F]FAZA (3 %, n = 1). Interestingly, metabolic stability *in vivo* looked different for [^{18}F]FBNA when compared to the metabolically very stable [^{18}F]FMISO and [^{18}F]FAZA.

After injection of [^{18}F]FBNA, two more polar radiometabolites were detected, and fractions of both radiometabolites increased over time.

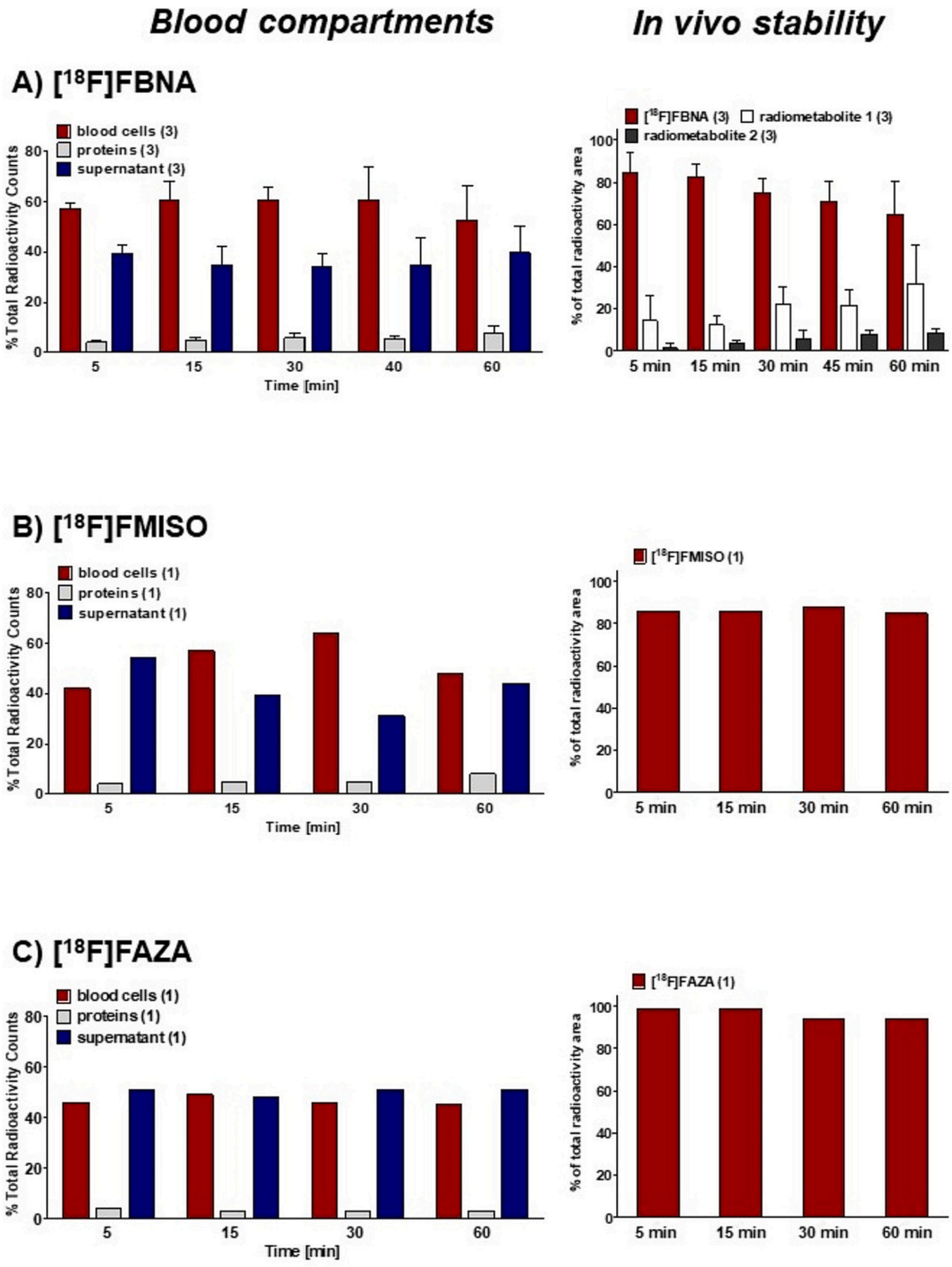

Fig. 3. Distribution of radioactivity in blood fractions (left) and metabolic stability over 60 min as determined from plasma samples (right) following injection of A) [^{18}F]FBNA, B) [^{18}F]FMISO and C) [^{18}F]FAZA into BALB/c mice. Data are shown as means ± SD from 3 experiments for [^{18}F]FBNA and 1 experiment for each [^{18}F]FAZA and [^{18}F]FMISO.

After 60 min post-injection 65 ± 9 % of intact [^{18}F]FBNA was detected, as well as 32 ± 11 % of radiometabolite 1 and 9 ± 1 % of radiometabolite 2 (all n = 3).

3.3. In vivo dynamic PET imaging

All three radiolabeled 2-nitroimidazoles were analyzed *in vivo* in estrogen receptor-positive MCF-7 and triple-negative MDA-MB231 tumours. Fig. 4 shows the PET images for [^{18}F]FBNA at 1 h, 2 h and 3 h post-injection.

Compared to [^{18}F]FBNA, radioactivity washout of [^{18}F]FMISO from muscle tissue was lower, and after 3 h post-injection, there was still a higher radioactivity level of [^{18}F]FMISO left in muscle tissue. However, radioactivity uptake of [^{18}F]FMISO into both MCF-7 and MDA-MB231 tumours was higher, and tumours became visible as early as 2 h p.i. (Fig. 5). A mainly hepatobiliary clearance pattern was observed for both, [^{18}F]FBNA and [^{18}F]FMISO.

Fig. 6 displays representative PET images after injection of [^{18}F]FAZA.

While tumour uptake of [^{18}F]FAZA into both tumour types was faster and more pronounced compared to [^{18}F]FBNA, radioactivity washout of [^{18}F]FAZA from muscle tissue was lower and rather more like that of [^{18}F]FMISO. Based on its lower lipophilicity [44], the clearance profile of [^{18}F]FAZA was slightly different, with a more pronounced renal clearance pattern compared to [^{18}F]FMISO and [^{18}F]FBNA.

Fig. 7 summarizes the time-activity curves (TACs) for the radiotracer uptake of all three radiolabeled 2-nitroimidazoles into MCF-7 and MDA-MB231 tumours and muscle tissue over 3 h.

Table 1 summarizes the SUV values for tumour and muscle uptakes and tumour-to-muscle ratios for the three radiotracers in the two animal models.

Interestingly, there were significant tumour tissue uptake differences for all three radiotracers between MCF-7 and MDA-MB231 tumours. At 5 min post-injection, all three radiolabeled 2-nitroimidazoles reached significantly higher uptake levels in MCF-7 *versus* MDA-MB231 tumour tissue as seen from the SUV values (Table 1). The observed trend of significant tumour uptake differences at early time points representing the perfusion phase (5 min p.i.) continued over the first hour of the dynamic PET experiments. However, it became less pronounced at later time points representing the metabolic phase (3 h p.i.) as seen from the SUV values at 180 min (Table 1). Over the entire 3 h time course, the overall tumour uptake increased significantly from 5 to 180 min p.i. after the injection of [^{18}F]FMISO (Δ89% in MCF-7 and Δ156% in MDA-MB231 tumours), and to a lesser extent for [^{18}F]FAZA (Δ22% in MCF-7 and Δ90% in MDA-MB231 tumours) being similar to that of [^{18}F]FBNA (Δ39% in MCF-7 and Δ100% in MDA-MB231 tumours).

The total tumour uptakes were always highest after injection of [^{18}F]FMISO, while they were similar for [^{18}F]FAZA and [^{18}F]FBNA. As shown in Table 1, radioactivity in muscle tissue was highest after 5 min post-injection and decreased over the 3 h time course through the washout of the radiotracers. Compared to [^{18}F]FAZA and [^{18}F]FBNA, [^{18}F]MISO resulted in the highest muscle uptake, with [^{18}F]FBNA showing slightly less muscle clearance after 3 h post-injection *versus* [^{18}F]FAZA. The resulting tumour-to-muscle ratios after 3 h were similar for [^{18}F]MISO and [^{18}F]FAZA in both tumours while being significantly lower for [^{18}F]FBNA (see Table 1).

3.4. Radiotracer kinetic analysis

Uptake and retention of [^{18}F]FBNA, [^{18}F]FMISO and [^{18}F]FAZA into MCF-7 and MDA-MB231 tumours were further analyzed by kinetic modelling using the established reversible two-tissue compartment model as described previously in the literature for [^{18}F]FAZA [31,48]. Cellular uptake of 2-nitroimidazoles is presumed to follow a two-step

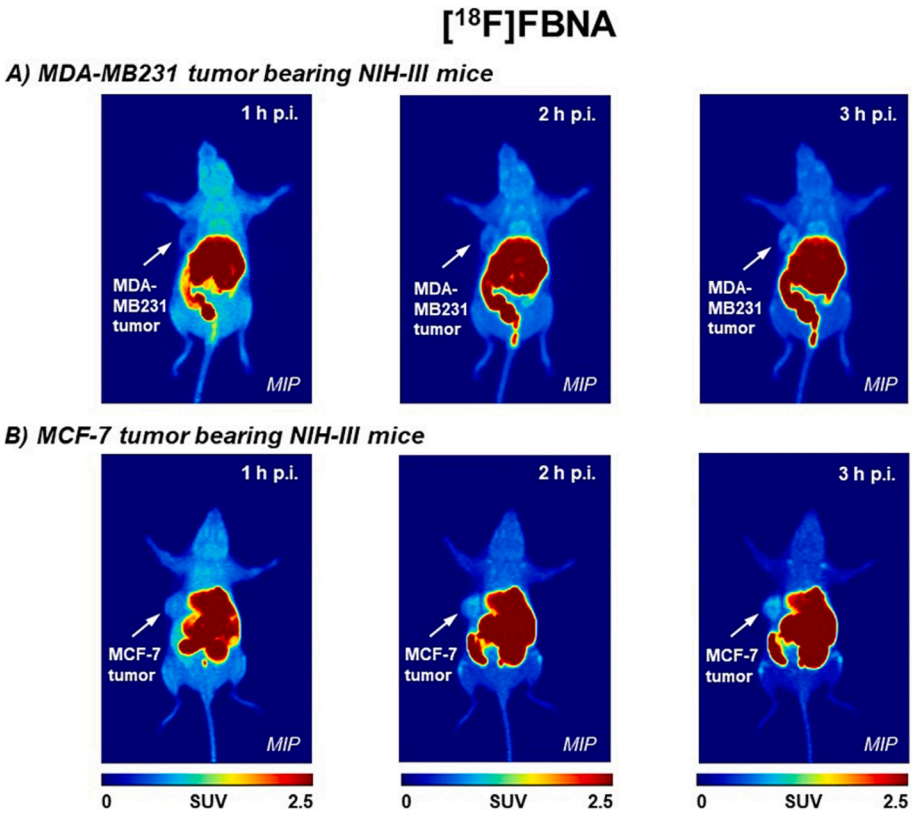

Fig. 4. Representative dynamic PET images after 1 h (summarized frames from 40 to 60 min), 2 h (summarized frames from 100 to 120 min) and 3 h (summarized frames from 160 to 180 min) post-injection of [^{18}F]FBNA into A) MDA-MB231 tumour-bearing NIH-III mice (23.6 g; 7.0 MBq; top) and B) MCF-7 tumour-bearing NIH-III mice (22.5 g; 6.0 MBq; bottom). MIP - Maximum Intensity Projection.

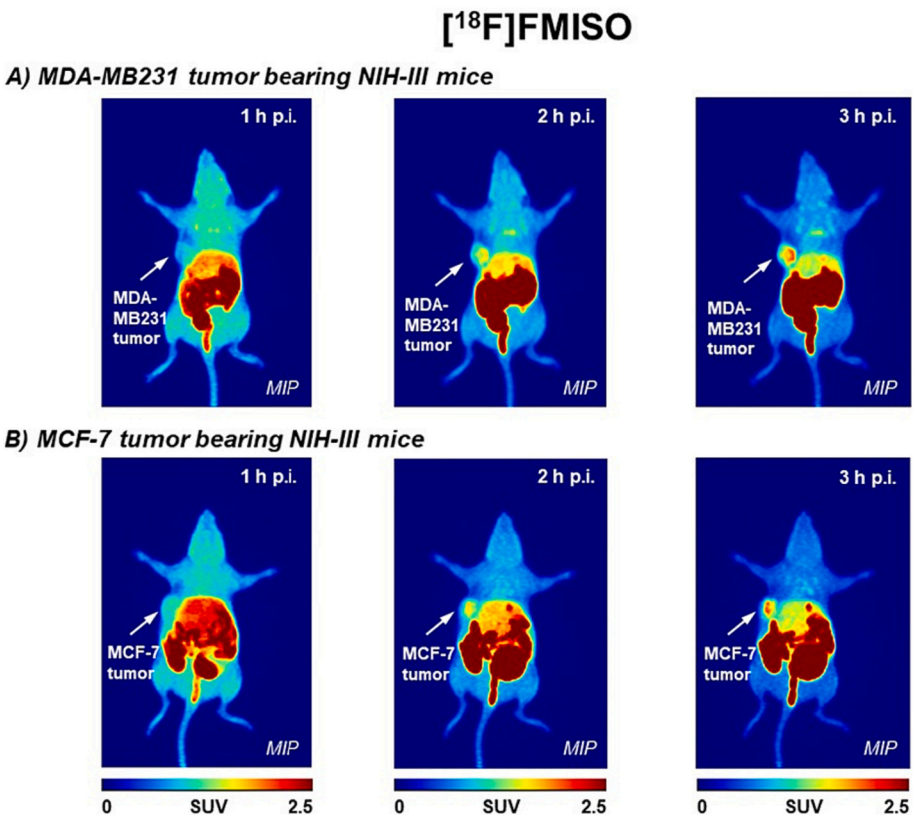

Fig. 5. Representative dynamic PET images after 1 h (summarized frames from 40 to 60 min), 2 h (summarized frames from 100 to 120 min) and 3 h (summarized frames from 160 to 180 min) post-injection of [^{18}F]FMISO into A) MDA-MB231 tumour-bearing NIH-III mice (23.9 g; 5.7 MBq; top) and B) MCF-7 tumour-bearing NIH-III mice (26.4 g; 6.3 MBq bottom). MIP - Maximum Intensity Projection.

process. The first step of passive transport through the cell membrane is described by kinetic parameters K1 (flux from the blood pool into the cell) and k2 (efflux from the cell to the blood pool). As a second step, intracellular trapping in and release from the 2nd compartment is described by kinetic parameters k3 and k4, respectively, commonly interpreted as chemical reduction and oxidation of the tracer.

Intracellular reduction of 2-nitroimidazoles by nitroreductases leads to the formation of reactive amines, resulting in their intracellular irreversible binding to different intracellular proteins in the cytoplasm. Kinetic parameters for all radiotracers and tumour models are summarized in Fig. 8.

Although rate constant K1 was comparable for all three radiotracers in MCF-7 tumours, MDA-MB231 tumours displayed a tendency for an elevated K1 value for [^{18}F]FMISO ((0.068 ± 0.006)/min (n = 4)) *versus* [^{18}F]FAZA ((0.048 ± 0.009)/min (n = 4)) (p = 0.0545) *versus* [^{18}F]FBNA ((0.034 ± 0.005)/min (n = 3)) (significant: $p < 0.01$), meaning that a potentially higher fraction of [^{18}F]FMISO was delivered to these tumours. However, the values for k2 followed the same trend, meaning that also more [^{18}F]FMISO than [^{18}F]FAZA and [^{18}F]FBNA was washed out from tumour tissue again. This led to a similar amount of [^{18}F]FBNA and [^{18}F]FAZA reaching the second compartment in MDA-MB231 tumours.

While the total amount of radiotracer entering the second compartment was similar within uncertainties for all three radiotracers in MDA-MB231 tumours, it was different in MCF-7 tumours, owing to differences in k3. This led to significantly different values of ratios k3/(k3 + k2) and K1*k3/(k3 + k2) (Fig. 8).

Values of k4 were significantly different from zero only for [^{18}F]FBNA in both tumour types, meaning that some amount of [^{18}F]FBNA was released again from the 2nd compartment. This was not the case for [^{18}F]FMISO and [^{18}F]FAZA (Fig. 8).

3.5. Autoradiography and immunohistochemistry

Uptake of [^{18}F]FBNA and [^{18}F]FMISO into MCF-7 and MDA-MB231 tumours was analyzed by autoradiography at 2 h post-injection and compared to HIF1α immunohistochemistry in the adjacent tumour tissue slices. However, due to limited availability, [^{18}F]FAZA was only measured in MDA-MB231 tumours. Fig. 9 summarizes the experimental results for the three analyzed radiotracers.

All three radiotracers showed higher radioactivity accumulation in certain tumour areas. Somewhat enriched [^{18}F]FBNA accumulation was detected in regions of elevated HIF-1α expression, especially in MDA-MB231 tumours. However, there were no systematic differences observed between the three radiotracers. All investigated tumour slices (MCF-7 and MDA-MB231) showed staining for HIF-1α. Taken together, no conclusive correlation could be observed between areas of high HIF-1a expression and regions with high radiotracer uptake. A possible correlation was seen for [^{18}F]FBNA uptake into MDA-MB231 tumours (Fig. 9).

3.6. Ex vivo biodistribution and dosimetry for [^{18}F]FBNA

Generating detailed dosimetry data is crucial for translating a novel PET radiotracer, such as [^{18}F]FBNA, into clinical applications [25]. To this end, a detailed *ex vivo* biodistribution experiment was carried out in female BALB/c mice at 5, 30 and 60 min and 3 and 6 h post-injection. Table 2 summarizes biodistribution data.

Except for the liver, radioactivity decrease was observed for all organs analyzed over the entire 6 h post-injection period. Substantial radioactivity levels were detected in the liver even at 6 h post-injection. Interestingly, just after the injection of [^{18}F]FBNA, a considerable amount of radioactivity was detected in the brain, indicating that this radiotracer readily crosses the blood-brain barrier.

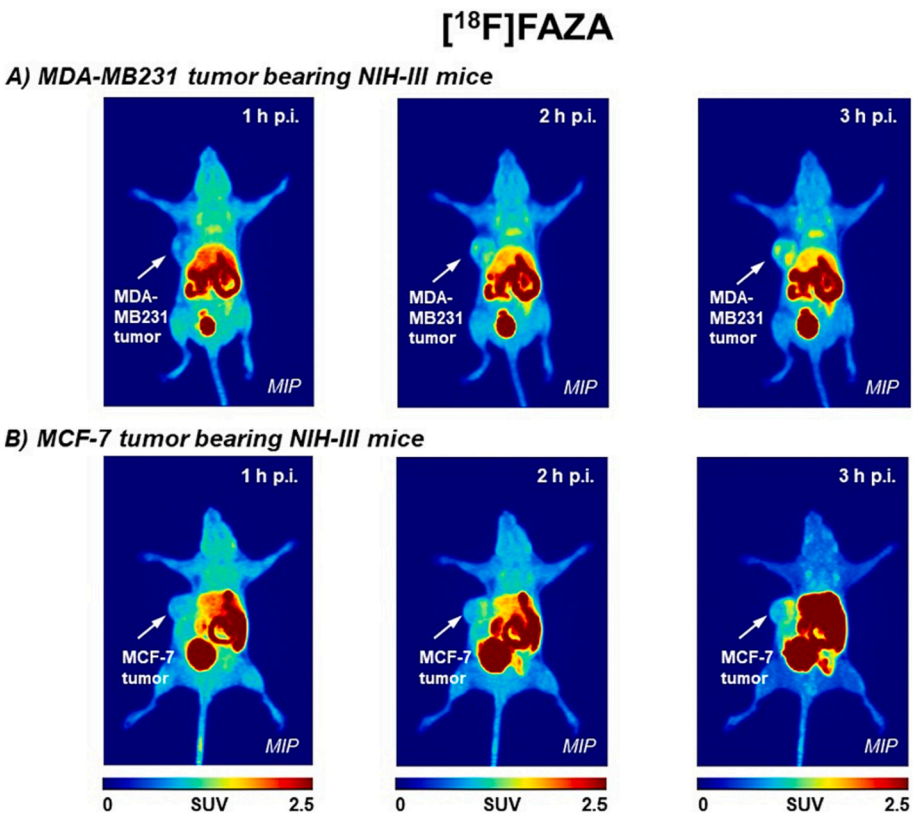

Fig. 6. Representative dynamic PET images after 1 h (summarized frames from 40 to 60 min), 2 h (summarized frames from 100 to 120 min) and 3 h (summarized frames from 160 to 180 min) post-injection of [^{18}F]FAZA into A) MDA-MB231 tumour-bearing NIH-III mice (23.3 g; 6.3 MBq; top) and B) MCF-7 tumour-bearing NIH-III mice (23.0 g; 5.5 MBq; bottom). MIP - Maximum Intensity Projection.

Table 3 summarizes the calculated human absorbed doses and effective dose for [^{18}F]FBNA as determined with OLINDA/EXM.

The highest absorbed doses resulted in the liver and the lower large intestinal (LLI) wall, corresponding to the high radioactivity detected in these areas during the PET experiments (Fig. 4). The resulting absorbed doses for the liver were 0.0374 mSv/MBq and 0.0470 mSv/MBq, and for the LLI wall, 0.0435 mSv/MBq and 0.0619 mSv/MBq for the human male and female, respectively.

The effective whole-body dose is 0.0230 mSv/MBq and 0.0352 mSv/MBq for the human adult male and female phantom. An assumed injected activity of 370 MBq (10 mCi) of [^{18}F]FBNA would expose an adult human male to 8.51 mSv and a human female to 13.02 mSv of effective radiation dose.

4. Discussion

The main findings of the present study are that: *(I)* 2-nitroimidazole [^{18}F]FBNA *in vitro* uptake into two different breast cancer cells follows a pattern similar to that of the established radiotracers [^{18}F]FMISO and [^{18}F]FAZA; *(II)* [^{18}F]FBNA shows *in vivo* breast cancer tumour uptake and retention similar to that of radiotracer [^{18}F]FAZA rather than [^{18}F]FMISO, however, with more noticeable differences in triple-negative MDA-MB231 than estrogen-receptor positive MCF-7 tumours; *(III)* based on its higher lipophilicity [^{18}F]FBNA, can cross the blood-brain barrier resulting to notable brain uptake; *(IV)* [^{18}F]FBNA also shows a sufficient background tissue clearance which allows for optimal image contrast. Based on all experimental data, [^{18}F]FBNA has a clear potential as a hypoxia PET imaging probe in a clinical setting.

The clinical value of imaging hypoxia in breast cancer is still being discussed. While it is well established that HIF-1α is overexpressed in triple-negative breast cancer [35–37], some uncertainty persists on whether hypoxia imaging markers such as ^{18}F-labeled 2-nitroimidazoles can measure differences between different phenotypes of breast cancers, possibly in part due to the lack of comparative studies. For historical reasons, there are still more studies available utilizing [^{18}F]FMISO than [^{18}F]FAZA [38].

While in other types of cancers, such as lung cancer, [^{18}F]FMISO has shown advantages [39], a multicenter study in head and neck cancer patients demonstrated similar advantages for [^{18}F]FMISO and [^{18}F]FAZA [40]. We have shown previously that [^{18}F]FAZA-PET could indicate differences between triple-negative MDA-MB231 and estrogen-receptor-positive MCF-7 tumour models when measured statically after 3 h post-injection [29]. However, differences were only significant for tumour-to-muscle ratios and not for tumour uptake data alone.

When measuring [^{18}F]FAZA uptake in the same tumour models dynamically, tumour uptake levels reached similar levels after 3 h post-injection indicating little differences in tumour uptake between triple-negative and estrogen-receptor-positive breast tumours. Systematic investigations using [^{18}F]FMISO and novel hypoxia imaging radiotracer [^{18}F]FBNA are now described in this study using the same breast cancer models during dynamic PET imaging experiments. All three ^{18}F-labeled 2-nitro-imidazoles, based on their passive diffusion as the primary uptake mechanism into tumour tissue, showed higher uptake in MCF-7 tumours *versus* MDA-MB231 tumours. This could be caused by differences in the perfusion characteristics between the two tumour models.

A recent clinical study in 29 breast cancer patients found a negative correlation between [^{18}F]FMISO-PET and perfusion markers determined by DCE-MRI [41]. All three 2-nitroimidazole-based radiotracers showed no washout of radioactivity from the tumour over the time course of the PET experiment in the two investigated breast tumour models. Noteworthy, PET imaging experiments with [^{18}F]FMISO and [^{18}F]FBNA indicated that both radiotracers showed potential at late time points (3 h post-injection) to differentiate between both breast cancer phenotypes. It would be important to demonstrate that these differences persist in a

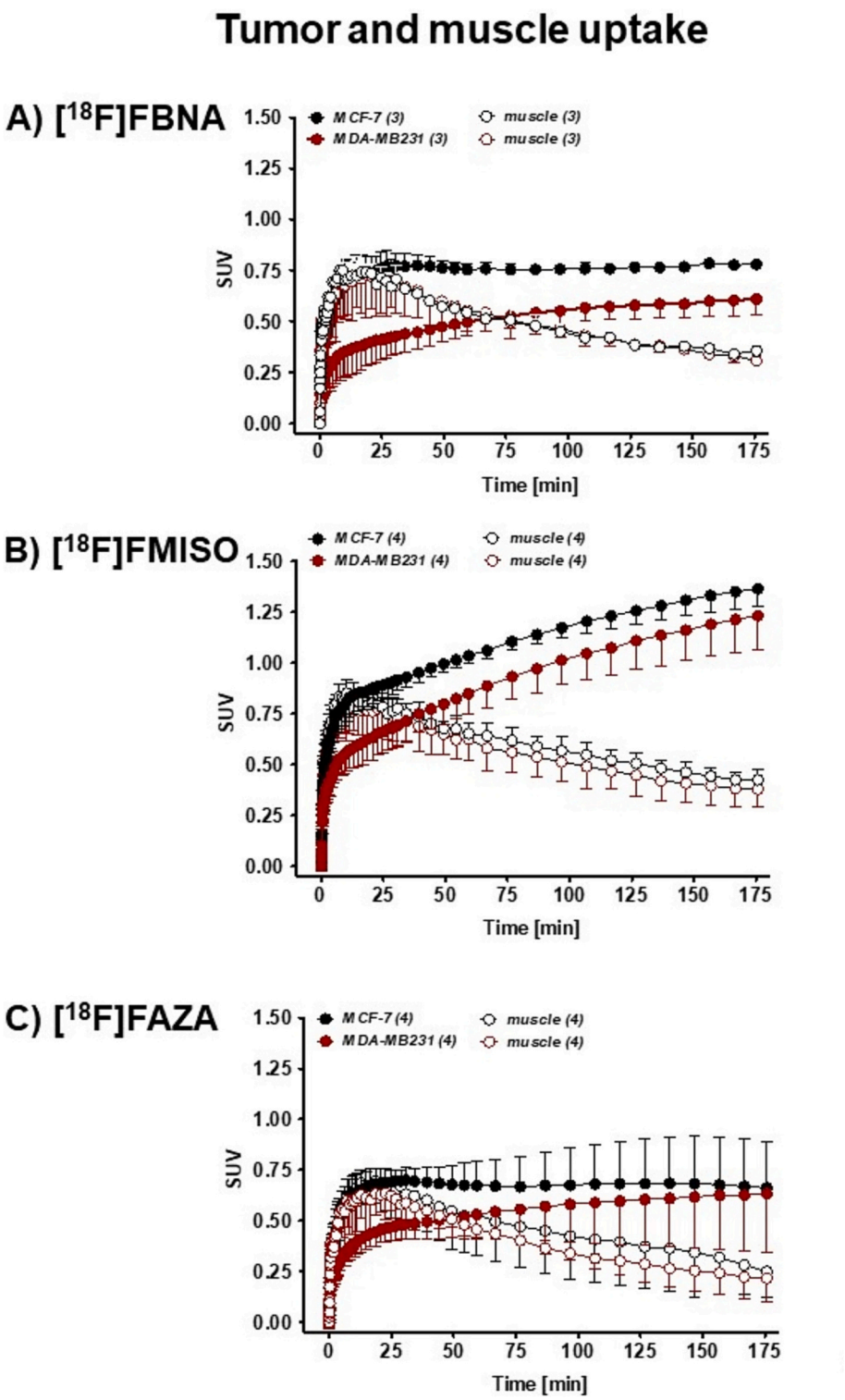

Fig. 7. Time-activity curves (TACs) over the entire time course (0–180 min post-injection) for kinetic analysis of radiotracer tumour uptake profiles *versus* non-targeting muscle tissue as background in MCF-7 and MDA-MB231 tumour-bearing NIH-III mice after injection of A) [^{18}F]FBNA, B) [^{18}F]FMISO and C) [^{18}F]FAZA. All data are shown as means ± SD from 3 to 4 individual experiments.

clinical setting and thus allow using differences in perfusion characteristics following radiotracer uptake studies to distinguish between both tumour types. Discussions are ongoing in the literature about 2-nitroimidazole PET imaging, tumour perfusion characteristics, and their fluctuations [42]. The accumulation of i.v. administered PET radiotracers strongly depend on their delivery to the target tissue or organ(*e.g.* tumour tissue). Low uptake of radiolabeled 2-nitroimidazoles may not be indicative of normoxic conditions, and the determination of tumour blood flow data may be required to rule out flow-limited delivery effects.

Instead, a high ^{18}F-labeled 2-nitroimidazole uptake could represent the presence of hypoxia caused by low oxygen supply, decreased diffusion capacity, or increased oxygen consumption [43]. Therefore, evaluating tumour hypoxia by imaging with ^{18}F-labeled 2-nitroimidazoles should always require careful consideration of context and additional

Table 1
SUV values for tumour and muscle uptake as well as tumour-to-muscle ratios (TMR) after injection of [^{18}F]FBNA, [^{18}F]FMISO and [^{18}F]FAZA into MCF-7 and MDA-MB231 tumour-bearing NIH-III mice. Data are derived from dynamic PET experiments and are shown as means ± SD from $n = 3$ or 4 experiments.

	[^{18}F] FBNA 5 min	[^{18}F] FBNA 180 min	[^{18}F] FMISO 5 min	[^{18}F] FMISO 180 min	[^{18}F] FAZA 5 min	[^{18}F] FAZA 180 min
n number	3	3	4	4	4	4
MCF-7 tumours	0.56 ± 0.11[a]	0.78 ± 0.02[d]	0.72 ± 0.07[b]	1.36 ± 0.09[e]	0.54 ± 0.11[c]	0.66 ± 0.23[f]
MDA-MB231 tumours	0.30 ± 0.12[a]	0.61 ± 0.08[d]	0.48 ± 0.07[b]	1.23 ± 0.17[e]	0.33 ± 0.05[c]	0.63 ± 0.29[f]
Muscle *(MCF-7 mice)*	0.69 ± 0.16	0.36 ± 0.01	0.79 ± 0.03	0.42 ± 0.05	0.58 ± 0.06	0.25 ± 0.12
Muscle *(MDA-MB231 mice)*	0.62 ± 0.19	0.31 ± 0.01	0.73 ± 0.12	0.38 ± 0.09	0.56 ± 0.14	0.22 ± 0.12
Tumour-to-muscle ratio *(MCF-7 mice)*	0.85 ± 0.30	2.19 ± 0.07[g,h]	0.90 ± 0.08	3.24 ± 0.30[g]	0.92 ± 0.14	2.92 ± 0.74[h]
Tumour-to-muscle ratio *(MDA-MB231 mice)*	0.50 ± 0.14	1.98 ± 0.26[i,j]	0.69 ± 0.24	3.32 ± 0.50[j]	0.61 ± 0.17	3.00 ± 0.42[i]

Values with the same letter were compared for significance: [a,b,c,d,g,i] $p < 0.05$; [j] $p < 0.01$; [e,f] n.s.

complementary experiments and data analysis. Nevertheless, pharmacodynamic and pharmacokinetic differences of ^{18}F-labeled 2-nitroimidazoles *in vivo* in the same morphologic breast cancer tumour model provide valuable additional information about the tumour microenvironment when imaging tumour hypoxia.

Our detailed kinetic data analysis comparing all three investigated ^{18}F-labeled 2-nitro-imidazoles, [^{18}F]FBNA, [^{18}F]FAZA and [^{18}F]FMISO, revealed that the fraction of 2-nitro-imidazole being trapped (moving from compartment 1 into compartment 2) is broadly similar within uncertainties for all three radiotracers in MDA-MB231 tumours, with the exception of significantly elevated values for [^{18}F]FMISO in MCF-7 tumours. However, even with significantly elevated [^{18}F]FMISO uptake (K1) into MDA-MB231 cells compared to [^{18}F]FAZA and [^{18}F]FBNA, the total amount of radiotracer contributing to the final "trapped = hypoxic" signal, K1*k3/(k2 + k3), is similar for all three radiotracers in MDA-MB231 tumours. Values for k3 were significantly >0 for all three 2-nitroimidazoles, which were therefore prone to enter the 2nd compartment resulting in binding. With values for k2 not significantly different among tracers, differences in k3 led to differences in trapped fractions (k3/(k2 + k3)) of the radiotracers. For MCF-7 tumours, the fraction k3/(k2 + k3) was elevated for [^{18}F]FMISO relative to [^{18}F]FAZA and [^{18}F]FBNA; since values of K1 were similar for all tracers in MCF-7 tumours, this led to a significant increase of trapped (bound) quantity of [^{18}F]FMISO in the tumour cells (K1*k3/(k2 + k3)). Together with the smaller value of k4, our findings suggest that [^{18}F]FMISO is the preferred PET radiotracer for imaging estrogen-receptor-positive MCF-7 tumours. However, when analyzing different types of breast cancer signatures, [^{18}F]FBNA and [^{18}F]FAZA show some advantages over [^{18}F]FMISO as both resulted in noticeable differences (Δ35–45 %) of the "trapping" amount (K1*k3/(k2 + k3)) *versus* Δ8–10 % for [^{18}F]FMISO when comparing MCF-7 and MDA-MB231 tumours.

The novel 2-nitroimidazole-based PET radiotracer [^{18}F]FBNA [25] acts similarly to the other radiolabeled 2-nitroimidazoles *in vitro*. [^{18}F]FBNA shows some metabolism in mice over the observed 60 min post-

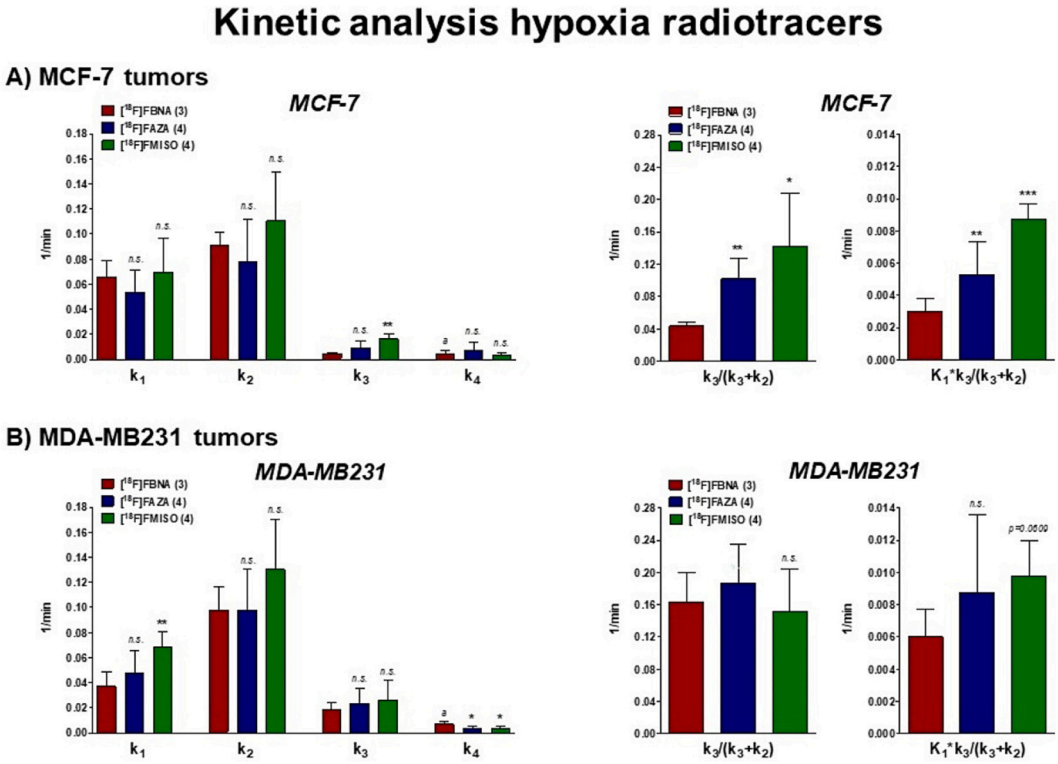

Fig. 8. Apparent tumour kinetic parameters K1 to k4 and ratios k3/(k2 + k3) and K1·(k3/(k2 + k3)) for [^{18}F]FBNA, [^{18}F]FMISO and [^{18}F]FAZA tumour uptake as derived from a two-tissue compartment model. A) top, MCF-7 tumours; B) bottom, MDA-MB231 tumours. Data are shown as mean ± SD from 3 to 4 experiments. * $p < 0.05$, ** $p < 0.01$, n.s. - not significant. [a] significant from 0 ($p < 0.05$).

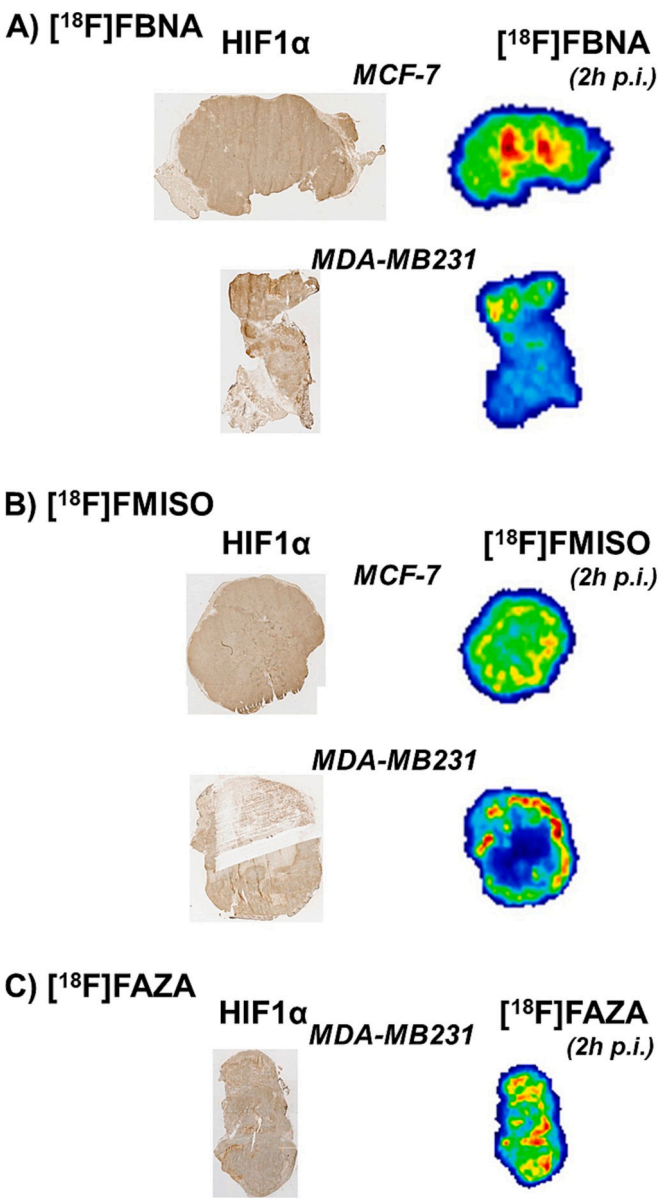

Fig. 9. Autoradiography analysis and HIF-1α immunohistochemistry (IHC) of excised MCF-7 and MDA-MB231 tumours at 2 h p.i. of A) [^{18}F]FBNA, B) [^{18}F]FMISO and C) [^{18}F]FAZA.

injection period. Its ability to cross the blood-brain barrier is similar to that of [^{18}F]FMISO and can be attributed due to the higher lipophilicity of [^{18}F]FBNA compared to [^{18}F]FMISO (log P 1.05 *versus* 0.36) [25]. Radiotracer uptake into the mouse brain reaches about 65 % of the [^{18}F]FMISO uptake levels after 30 min [44]. In contrast, [^{18}F]FAZA (log P -0.43 [25]) can only cross the disrupted blood-brain barrier, as in glioma patients [20]. In contrast, even with its higher lipophilicity [^{18}F]FBNA still possesses sufficient muscle tissue clearance, *i.e.* ~50 % less radioactivity in muscle tissue than [^{18}F]FMISO after 60 min [44] and even ~80 % lower radioactivity in the muscle compared to [^{18}F]FMISO after 3 h post-injection [45]. This may contribute to a better image contrast *versus* [^{18}F]FMISO as seen in the mouse PET images, and it would be similar to [^{18}F]FAZA, which is known for a better and faster non-target tissue clearance profile than [^{18}F]FMISO [46]. An autoradiographic analysis of HIF-1α immunohistochemical staining suggests higher [^{18}F]FBNA accumulation in regions of elevated HIF-1α expressing regions in the MDA-MB231 tumours. However, this trend was not systematic in MCF-7 tumours and for [^{18}F]FMISO and [^{18}F]FAZA and would require additional experiments and clarification. As discussed, limitations in radiotracer delivery to the tumour tissue may contribute to the observed differences between radiotracer uptake and HIF-1α expression in tumour tissues.

Table 2
Biodistribution of [^{18}F]FBNA in female BALB/c mice. Data are shown as means ± SD %ID/g from $n = 4$ experiments.

	5 min	30 min	60 min	3 h	6 h
n number	4	4	4	4	4
Organ					
Blood	7.34 ± 2.14	4.67 ± 0.37	3.22 ± 0.82	0.89 ± 0.09	0.37 ± 0.02
Heart	9.66 ± 3.03	5.70 ± 0.32	3.73 ± 0.83	0.86 ± 0.06	0.31 ± 0.02
Lung	7.86 ± 2.52	4.86 ± 0.46	3.58 ± 0.83	0.99 ± 0.06	0.36 ± 0.06
Liver	18.73 ± 6.15	19.99 ± 1.67	18.26 ± 4.43	19.37 ± 3.21	15.53 ± 1.56
Kidney (right)	10.94 ± 2.62	7.64 ± 1.52	5.59 ± 1.64	2.02 ± 0.39	0.64 ± 0.07
Kidney (left)	11.32 ± 2.23	8.04 ± 0.36	6.83 ± 1.58	2.18 ± 0.20	0.63 ± 0.06
Spleen	8.51 ± 3.02	4.45 ± 0.14	2.81 ± 0.58	0.65 ± 0.05	0.25 ± 0.05
Stomach	5.71 ± 2.28	3.84 ± 1.19	3.12 ± 0.44	1.33 ± 0.20	0.30 ± 0.14
Duodenum	14.02 ± 5.96	17.43 ± 7.56	5.46 ± 1.20	1.87 ± 0.51	0.66 ± 0.11
Small intestine	11.97 ± 3.72	25.61 ± 5.11	26.94 ± 7.01	5.47 ± 1.39	1.07 ± 0.18
Upper large intestine	8.57 ± 2.86	6.73 ± 1.28	3.91 ± 0.77	8.24 ± 1.21	1.17 ± 0.14
Lower large intestine	7.40 ± 2.07	12.91 ± 0.70	15.76 ± 4.21	46.93 ± 4.92	19.44 ± 7.11
Pancreas	8.16 ± 2.72	4.36 ± 0.74	2.67 ± 0.39	0.69 ± 0.17	0.19 ± 0.02
Bone	1.68 ± 0.50	1.06 ± 0.36	0.56 ± 0.27	0.34 ± 0.04	0.38 ± 0.08
Muscle	3.24 ± 0.91	3.38 ± 0.72	2.02 ± 0.35	0.37 ± 0.06	0.12 ± 0.03
Ovaries	5.21 ± 1.61	3.19 ± 0.68	1.69 ± 0.54	0.67 ± 0.15	0.35 ± 0.13
Brain	4.10 ± 1.74	2.88 ± 0.62	1.96 ± 0.28	0.57 ± 0.44	0.09 ± 0.01
Fat	0.95 ± 0.13	1.34 ± 0.27	0.83 ± 0.17	0.20 ± 0.06	0.07 ± 0.01
Thymus	5.70 ± 2.47	3.02 ± 0.69	2.07 ± 0.82	0.55 ± 0.09	0.21 ± 0.04
Uterus	4.63 ± 0.92	3.65 ± 1.08	2.81 ± 0.63	1.02 ± 0.35	0.42 ± 0.20
Urinary bladder	5.32 ± 2.16	4.99 ± 1.77	3.03 ± 1.11	1.07 ± 0.65	0.43 ± 0.19
Urine	9.24 ± 4.06	129.83 ± 68.12	187.08 ± 132.6	154.86 ± 74.69	82.80 ± 69.92

Nevertheless, a systematic analysis in a model of rheumatoid arthritis, which is associated with hypoxia in these inflamed regions, showed that both [^{18}F]FMISO and [^{18}F]FAZA exhibit an increased uptake in the areas related to elevated HIF-1α expression [47]. This observation may also be relevant for studying tumour hypoxia with 2-nitroimidazole radiotracers, as exemplified in this study using preclinical breast cancer models.

In conclusion, we have characterized the radiopharmacological profile of novel ^{18}F-radiolabeled 2-nitroimidazole [^{18}F]FBNA *in vitro* and *in vivo;* and performed a systematic comparison with [^{18}F]FMISO and [^{18}F]FAZA for imaging in two types of preclinical breast cancer models. With the complete dosimetry data set generated here for [^{18}F]FBNA, this novel radiotracer could be used for first-in-human clinical study. It may be of interest to analyze [^{18}F]FBNA in a clinical setting alongside [^{18}F]FMISO and [^{18}F]FAZA and determine its potential value for imaging breast cancer and other solid cancer and tissue hypoxia. However, we also want to emphazise again that PET imaging with 2-nitroimidazole

Table 3
Predicted human absorbed doses for [^{18}F]FBNA.

Absorbed doses	Injected activity		370	MBq
	Male		Female	
	mSv/MBq	mSv	mSv/MBq	mSv
Adrenals	9.73E-03	3.60	1.27E-02	4.70
Brain	4.28E-03	1.58	5.58E-03	2.06
Breasts	5.49E-03	2.03	7.26E-03	2.69
Gallbladder Wall	1.36E-02	5.03	1.68E-02	6.22
LLI Wall	4.35E-02	16.10	6.19E-02	22.90
Small Intestine	1.92E-02	7.10	2.69E-02	9.95
Stomach Wall	1.54E-02	5.70	2.16E-02	7.99
ULI Wall	1.74E-02	6.44	2.48E-02	9.18
Heart Wall	9.56E-03	3.54	1.23E-02	4.55
Kidneys	2.04E-02	7.55	2.61E-02	9.66
Liver	3.74E-02	13.84	4.70E-02	17.39
Lungs	8.51E-03	3.15	1.12E-02	4.14
Muscle	7.50E-03	2.78	9.93E-03	3.67
Ovaries	1.42E-02	5.25	2.10E-02	7.77
Pancreas	1.13E-02	4.18	1.46E-02	5.40
Red Marrow	6.98E-03	2.58	9.29E-03	3.44
Osteogenic Cells	8.83E-03	3.27	1.24E-02	4.59
Skin	5.03E-03	1.86	6.72E-03	2.49
Spleen	8.94E-03	3.31	1.18E-02	4.37
Testes	8.99E-03	3.33		
Thymus	6.41E-03	2.37	8.52E-03	3.15
Thyroid	5.94E-03	2.20	7.32E-03	2.71
UB Wall	1.61E-01	59.57	2.88E-01	106.56
Uterus	1.91E-02	7.07	2.68E-02	9.92
Total Body	9.09E-03	3.36	1.22E-02	4.51
Effective Dose:	2.30E-02	8.51	3.52E-02	13.02

radiotracers such as [^{18}F]FBNA, [^{18}F]FMISO, and [^{18}F]FAZA does not allow for the direct measurement of tissue hypoxia, which in general represents a significant limitation of this entire class of compounds.

Declaration of competing interest

The authors declare that they have no known competing financial interests or personal relationships that could have appeared to influence the work reported in this paper.

Acknowledgements

The authors thank David Clendening, Loyd Baker, and Blake Lazurko from the Edmonton Radiopharmaceutical Center (ERC) for ^{18}F production and the excellent technical support during radiopharmaceutical synthesis procedures. We thank Dan McGinn from the Vivarium of the Cross Cancer Institute (Edmonton, Alberta) for supporting the animal work. In addition, Dr. Sofia Nascimento dos Santos would like to thank the International Atomic Energy Agency (IAEA) for a scholarship during her visit of the preclinical PET imaging facility of the Department of Oncology at the University of Alberta (Edmonton, Canada).

References

[1] Rakotomalala A, Escande A, Furlan A, Meignan S, Lartigau E. Hypoxia in solid tumors: how low oxygenation impacts the "Six Rs" of radiotherapy. Front Endocrinol (Lausanne) 2021;12:742215.
[2] Thureau S, Dubray B, Modzelewski R, Bohn P, Hapdey S, Vincent S, et al. FDG and FMISO PET-guided dose escalation with intensity-modulated radiotherapy in lung cancer. Radiat Oncol 2018;13:208.
[3] Horsman MR, Vaupel P. Pathophysiological basis for the formation of the tumor microenvironment. Front Oncol 2016;12(6):66.
[4] Muz B, de la Puente P, Azab F, Azab AK. The role of hypoxia in cancer progression, angiogenesis, metastasis, and resistance to therapy. Hypoxia (Auckl) 2015;3:83–92.
[5] Albiach CF, Moreno AC, Cordon MR, Morillo Macías V, Bouché Babiloni A, Beato Tortajada I, et al. Contribution of hypoxia-measuring molecular imaging techniques to radiotherapy planning and treatment. Clin Transl Oncol 2010;12:22–6.
[6] Semenza GL. Molecular mechanisms mediating metastasis of hypoxic breast cancer cells. Trends Mol Med 2012;18:534–43.
[7] Sun X, Niu G, Chan N, Shen B, Chen X. Tumor hypoxia imaging. Mol Imaging Biol 2011;13:399–410.
[8] Abadjian MZ, Edwards WB, Anderson CJ. Imaging the Tumor Microenvironment. Adv Exp Med Biol 2017;1036:229–57.
[9] Lopci E, Grassi I, Chiti A, Nanni C, Cicoria G, Toschi L, et al. PET radiopharmaceuticals for imaging of tumor hypoxia: a review of the evidence. Am J Nucl Med Mol Imaging 2014;4:365–84.
[10] Rickard AG, Palmer GM, Dewhirst MW. Clinical and preclinical methods for quantifying tumor hypoxia. Adv Exp Med Biol 2019;1136:19–41.
[11] Wuest M, Wuest F. Positron emission tomography radiotracers for imaging hypoxia. J Labelled Comp Radiopharm 2013;56:244–50.
[12] Rajendran JG, Krohn KA. F-18 fluoromisonidazole for imaging tumor hypoxia: imaging the microenvironment for personalized cancer therapy. Semin Nucl Med 2015;45:151–62.
[13] Xu Z, Li XF, Zou H, Sun X, Shen B. ^{18}F-Fluoromisonidazole in tumor hypoxia imaging. Oncotarget. 2017;8:94969–79.
[14] Hirata K, Yamaguchi S, Shiga T, Kuge Y, Tamaki N. The roles of hypoxia imaging using ^{18}F-Fluoromisonidazole positron emission tomography in glioma treatment. J Clin Med 2019;8:1088.
[15] Lee NY, Mechalakos JG, Nehmeh S, Lin Z, Squire OD, Cai S, et al. Fluorine- 18-labeled fluoromisonidazole positron emission and computed tomography-guided intensity-modulated radiotherapy for head and neck cancer: a feasibility study. Int J Radiat Oncol Biol Phys 2008;70:2–13.
[16] Krohn KA, Link JM, Mason RP. Molecular imaging of hypoxia. J Nucl Med 2008;49 (Suppl. 2) (129S-48S).
[17] Kumar P, Stypinski D, Xia H, McEwan AJB, Machulla HJ, Wiebe LI. Fluoroazomycin arabino- side (FAZA): synthesis, H-2 and H-3-labelling and preliminary biological evaluation of a novel 2-nitroimidazole marker of tissue hypoxia. J Label Compd Radiopharm 1999;42:3–16.
[18] Busk M, Munk OL, Jakobsen S, Wang T, Skals M, Steiniche T, et al. Assessing hypoxia in animal tumor modls based on pharmacokinetic analysis of dynamic FAZA PET. Acta Oncol 2010;49:922–33.
[19] Souvatzoglou M, Grosu AL, Roeper B, Krause BJ, Beck R, Reischl G, et al. Tumour hypoxia imaging with [^{18}F]FAZA PET in head and neck cancer patients: a pilot study. Eur J Nucl Med Mol Imaging 2007;34:1566–75.
[20] Postema EJ, McEwan AJ, Riauka TA, Kumar P, Richmond DA, Abrams DN, et al. Initial results of hypoxia imaging using 1-alpha-D: -(5-deoxy-5-[18F]-fluoroarabinofuranosyl)-2-nitroimidazole (^{18}F-FAZA). Eur J Nucl Med Mol Imaging 2009;36:1565–73.
[21] Hu M, Xie P, Lee NY, Li M, Ho F, Lian M, et al. Hypoxia with ^{18}F-fluoroerythronitroimidazole integrated positron emission tomography and computed tomography (^{18}F-FETNIM PET/CT) in locoregionally advanced head and neck cancer: hypoxia changes during chemoradiotherapy and impact on clinical outcome. Medicine (Baltimore) 2019;98:e17067.
[22] Barthel H, Wilson H, Collingridge DR, Brown G, Osman S, Luthra SK, et al. In vivo evaluation of [^{18}F]fluoroetanidazole as a new marker for imaging tumour hypoxia with positron emission tomography. Br J Cancer 2004;90:2232–42.
[23] Eskola O, Gronross TJ, Forsback S, Tuomela J, Komar G, Bergman J, et al. Tracer level electrophilic synthesis and pharmacokinetics of the hypoxia tracer [(18)F] EF5. Mol Imaging Biol 2012;14:205–12.
[24] Fleming IN, Manavaki R, Blower PJ, West C, Williams KJ, Harris AL, et al. Imaging tumour hypoxia with positron emission tomography. Br J Cancer 2015;112:238–50.
[25] Nario AP, Woodfield J, Nascimento dos Santos S, Bergman C, Wuest M, Araujo YB, et al. Synthesis of a 2-nitroimidazole derivative N-(4-[^{18}F]fluoro-benzyl)-2-(2-nitro-1H-imidazol-1-yl)-acetamide ([^{18}F]FBNA) as PET radiotracer for imaging tumor hypoxia. EJNMMI Radiopharm Chem 2022;7:13.
[26] Li Q, Lin Q, Yun Z. Hypoxia-activated cytotoxicity of benznidazole against clonogenic tumor cells. Cancer Biol Ther 2016;17:1266–73.
[27] Reischl G, Ehrlichmann W, Bieg C, Solbach C, Kumar P, Wiebe LI, et al. Preparation of the hypoxia imaging PET tracer [^{18}F]FAZA: reaction parameters and automation. Appl Radiat Isot 2005;62:897–901.
[28] Oh SJ, Chi DY, Mosdzianowski C, Kim JY, Gil HS, Kang SH, et al. Fully automated synthesis of [^{18}F]fluoromisonidazole using a conventional [^{18}F] FDG module. Nucl Med Biol 2005;32(8):899–905.
[29] Hamann I, Krys D, Glubrecht D, Bouvet V, Marshall A, Vos L, et al. Expression and function of hexose transporters GLUT1, GLUT2, and GLUT5 in breast cancer-effects of hypoxia. FASEB J 2018;32:5104–18.
[30] Goertzen AL, Bao Q, Bergeron M, Blankemeyer E, Blinder S, Cañadas M, et al. NEMA NU 4-2008 comparison of preclinical PET imaging systems. J Nucl Med 2012;53(8):1300–9.
[31] Verwer EE, van Velden FHP, Bahce I, Yaqub M, Schuit RC, Windhorst AD, et al. Pharmacokinetic analysis of [^{18}F]FAZA in non-small cell lung cancer patients. Eur J Nucl Med Mol Imaging 2013;40:1523–31.
[32] Stabin MG, Sparks RB, Crowe E. OLINDA/EXM: the second-generation personal computer software for internal dose assessment in nuclear medicine. J Nucl Med 2005;46:1023–7.
[33] Basic anatomical and physiological data for use in radiological protection: reference values. A report of age- and gender-related differences in the anatomical and physiological characteristics of reference individuals. In: ICRP Publication 89. vol. 32. Ann ICRP; 2002. p. 5–265.
[34] Stabin M, Emmons MA, Segars WP, Fernald M, Brill AB. ICRP-89 based adult and pediatric phantom series. J Nucl Med 2008;49(Suppl. 1):14P.
[35] Wuest M, Kuchar M, Sharma SK, Richter S, Hamann I, Wang M, et al. Targeting lysyl oxidase for molecular imaging in breast cancer. Breast Cancer Res 2015;17:107.

[36] Nedeljković M, Damjanović A. Mechanisms of chemotherapy resistance in triple-negative breast cancer—how we can rise to the challenge. Cells. 2019;8:957.
[37] Nath A, Mitra S, Mistry T, Pal R, Nasare VD. Molecular targets and therapeutics in chemoresistance of triple-negative breast cancer. Med Oncol 2021;39:14.
[38] Li H, Liu Z, Yuan L, Fan K, Zhang Y, Cai W, et al. Radionuclide-based imaging of breast cancer: state of the art. Cancers (Basel) 2021;13:5459.
[39] Thureau S, Piton N, Gouel P, Modzelewski R, Dujon A, Baste JM, et al. First comparison between [^{18}F]-FMISO and [^{18}F]-Faza for preoperative pet imaging of hypoxia in lung cancer. Cancers (Basel) 2021;13:4101.
[40] Zschaeck S, Löck S, Hofheinz F, Zips D, Saksø Mortensen L, Zöphel K, et al. Individual patient data meta-analysis of FMISO and FAZA hypoxia PET scans from head and neck cancer patients undergoing definitive radio-chemotherapy. Radiother Oncol 2020;149:189–96.
[41] Carmona-Bozo JC, Manavaki R, Woitek R, Torheim T, Baxter GC, Caracò C, et al. Hypoxia and perfusion in breast cancer: simultaneous assessment using PET/MR imaging. Eur Radiol 2021;31:333–44.
[42] Kimura H, Braun RD, Ong ET, Hsu R, Secomb TW, Papahadjopoulos D, et al. Fluctuations in red cell flux in tumor microvessels can lead to transient hypoxia and reoxygenation in tumor parenchyma. Cancer Res 1996;56:5522–8.
[43] Iqbal R, Kramer GM, Verwer EE, Huisman MC, de Langen AJ, Bahce I, et al. Multiparametric analysis of the relationship between tumor hypoxia and perfusion with ^{18}F-fluoroazomycin arabinoside and ^{15}O-H_2O PET. J Nucl Med 2016;57:530–5.
[44] Zhang L, Yao X, Cao J, Hong H, Zhang A, Zhao R, et al. In vivo ester hydrolysis as a new approach in development of positron emission tomography tracers for imaging hypoxia. Mol Pharm 2019;16:1156–66.
[45] Reischl G, Dorow DS, Cullinane C, Katsifis A, Roselt P, Binns D, et al. Imaging of tumor hypoxia with [^{124}I]IAZA in comparison with [^{18}F]FMISO and [^{18}F]FAZA–first small animal PET results. J Pharm Pharm Sci 2007;10:203–11.
[46] Piert M, Machulla HJ, Picchio M, Reischl G, Ziegler S, Kumar P, et al. Hypoxia-specific tumor imaging with ^{18}F-fluoroazomycin arabinoside. J Nucl Med 2005;46:106–13.
[47] Fuchs K, Kuehn A, Mahling M, Guenthoer P, Hector A, Schwenck J, et al. In vivo hypoxia PET imaging quantifies the severity of arthritic joint inflammation in line with overexpression of hypoxia-inducible factor and enhanced reactive oxygen species generation. J Nucl Med 2017;58:853–60.
[48] Chapman DW, Jans HS, Ma I, Mercer JR, Wiebe LI, Wuest M, et al. Detecting functional changes with [(^{18})F]FAZA in a renal cell carcinoma mouse model following sunitinib therapy. EJNMMI Res 2014;4(1):27.
[49] Jans HS, Yang XH, Brocks DR, Kumar P, Wuest M, Wiebe LI. Positron emission tomography (PET) and pharmacokinetics: classical blood sampling versus image-derived analysis of [18F]FAZA and [18F]FDG in a murine tumor bearing model. J Pharm Pharm Sci 2018;21(1s):32s–47s.